

Coherent driving of Tm^{3+} :YAG ions using a complex hyperbolic secant optical field

F. de Seze, F. Dahes, V. Crozatier, I. Lorgeré, F. Bretenaker, and J.-L. Le Gouët^a

Laboratoire Aimé Cotton, Centre National de la Recherche Scientifique, Bâtiment 505, Campus Universitaire, 91405 Orsay, France

Received 19 January 2005

Published online 15 June 2005 – © EDP Sciences, Società Italiana di Fisica, Springer-Verlag 2005

Abstract. We investigate the coherent driving of atomic systems by Complex Hyperbolic Secant (CHS) pulses in optical domain. First, with the help of a Rapid Adiabatic Passage approach we get physical insight into the process. We discuss the limiting factors on spectral selectivity and transfer efficiency, such as finite coherence lifetime and excitation finite duration. Then, with a highly-stabilized cw laser and fast electronic equipment, we experimentally explore the CHS process at μs -timescale in a Tm^{3+} :YAG crystal. We demonstrate efficient adiabatic transfer over a few hundreds of kHz-wide spectral interval within the inhomogeneous linewidth. We calculate and detect the Free Induction Decay signal as the signature of the atomic coherences during the process.

PACS. 42.50.Md Optical transient phenomena: quantum beats, photon echo, free-induction decay, dephasings and revivals, optical nutation, and self-induced transparency – 32.80.Qk Coherent control of atomic interactions with photons – 03.67.Lx Quantum computation

1 Introduction

Rare earth ions embedded into inorganic crystals have been recently considered in the field of quantum information [1–3]. They offer very long coherence lifetimes: optical coherence times, up to 2.6 ms [4], and coherence times in the ground state nuclear spin transitions, up to 80 ms [5], have been observed. The optical transitions, with homogeneous linewidth of the order of kHz, are inhomogeneously broadened up to several tenths of GHz, offering a very large number of frequency channels. The ions embedded in the crystals exhibit a large static dipole moment, allowing dipole-dipole interaction between ions that belong to different frequency channels [1].

To achieve quantum computing operations, as the C-NOT gate proposed in [1], we have to coherently drive all the ions belonging to a frequency channel. Hard pulses [6] are not robust against the frequency variations inside a frequency channel. They are not robust either against the Rabi frequency inhomogeneities due to the field absorption during the propagation through the material, and due to the different orientations of the transition dipoles in the different sites of the crystal. Composite pulses have been recently proposed to improve the hard pulses robustness [7].

Rapid Adiabatic Passage (RAP) is known to be robust against experimental parameter variations. In this paper, we focus on a RAP process based on Complex Hyperbolic Secant (CHS) pulses that is commonly used in NMR [8]. These pulses are able to achieve efficient, frequency selective adiabatic transfer within an inhomogeneously broadened ensemble of atoms. CHS pulses have also been studied in the field of coherent optics at femtosecond timescale [9–11] where population inversion was experimentally observed. Zero dispersion lines were used to shape the femtosecond CHS [11]. In Tm^{3+} :YAG, coherent driving is operated at μs timescale which opens the way to efficient electronic modulation techniques. At this timescale, a high-stability laser is required. We have built a source that offers a linewidth of 250 Hz over the 10 ms process duration and, for the first time in optical domain, we were able to demonstrate >80% coherent population transfer using a CHS pulse [12]. In the present work we take advantage of our high-precision set-up to thoroughly investigate CHS excitation both theoretically and experimentally. The theoretical study relies on an adiabatic description of the Bloch vector motion.

In Section 2, we present RAP basics. Section 3 is devoted to the theoretical discussion of CHS population transfer. The corresponding experimental results are presented in Section 4. The behavior of atomic coherence under CHS excitation is examined in Section 5 in the prospect of experimental Free Induction Decay observation, which is presented in Section 6.

^a e-mail: jean-louis.legouet@lac.u-psud.fr

2 Adiabatic passage with a linearly swept monochromatic laser

A two-level atom is conveniently described by the level population difference $n_{21} = n_2 - n_1$ and by the off-diagonal density matrix element ρ_{12} . The atom interacts with a classical electric field defined as:

$$E(t) = \mathcal{E}(t)e^{2i\pi\nu_0 t + i\varphi(t)} + cc \quad (1)$$

where $\varphi(t_0) = 0$ and $\dot{\varphi}(t_0) = 0$ and $\mathcal{E}(t)$ is a real quantity. The field is close to resonance with the electric dipole transition at ν_{12} . Coupling with the electric field is characterized by the Rabi frequency, defined as the product of the field amplitude and the optical dipole moment d_{ab} , divided by the Planck constant \hbar :

$$\Omega(t) = \frac{d_{ab}\mathcal{E}(t)}{\hbar}. \quad (2)$$

In the absence of relaxation, the atomic system evolution is given in the rotating wave approximation by the density matrix equations [15]:

$$\begin{aligned} \frac{dn_{21}}{dt} &= i\Omega(\tilde{\rho}_{12} - \tilde{\rho}_{21}) \\ \frac{d\tilde{\rho}_{12}}{dt} &= \frac{i\Omega}{2}n_{21} - i[\Delta + \dot{\varphi}(t)]\tilde{\rho}_{12} \end{aligned} \quad (3)$$

where $\Delta = 2\pi(\nu_0 - \nu_{12})$ and

$$\tilde{\rho}_{12} = \rho_{12}e^{-2i\pi\nu_0(t-t_0) - i\varphi(t)}. \quad (4)$$

The atomic state can be represented by a three component vector, the Bloch vector $\vec{B}(u, v, w)$. The horizontal components u and v respectively represent the real and imaginary part of $\tilde{\rho}_{12}$:

$$\begin{aligned} u &= \rho_{12} + \tilde{\rho}_{21} \\ v &= i(\tilde{\rho}_{21} - \tilde{\rho}_{12}). \end{aligned} \quad (5)$$

The vertical component w represents the population difference:

$$w = n_{12}. \quad (6)$$

In the absence of relaxation, the Bloch vector head evolves on a sphere of unit radius, called Bloch sphere. The density matrix equation can be converted into the following precession equation of the Bloch vector around the driving vector $\vec{D}(\Omega, 0, \Delta + \dot{\varphi}(t))$:

$$\frac{d\vec{B}}{dt} = -\vec{D} \wedge \vec{B}. \quad (7)$$

In the context of quantum information, we need prepare a two-level atom in an arbitrary superposition state, i.e. direct the Bloch vector in an arbitrary orientation. An elementary example of Bloch vector control is the π rotation from downward to upward direction corresponding to state swapping. The Bloch vector flipping is efficiently achieved with the help of a fixed amplitude, infinite duration, frequency swept field that resonantly interacts at

time $t = t_0$. The laser frequency is linearly swept at chirp rate r according to:

$$\dot{\varphi}(t) = 2\pi r(t - t_0). \quad (8)$$

Initially the electric field exhibits a detuning $\Delta + \dot{\varphi}(-\infty) = -\infty$. The corresponding driving vector \vec{D} is vertical, downward oriented. As time elapses, the detuning increases which makes \vec{D} rotate around Ov -axis until \vec{D} is finally vertical, upward oriented. The vertical component of \vec{D} vanishes at resonance and \vec{D} flips on a timescale of Ω/r . Initially the ground state atomic Bloch vector is also vertical, downward oriented on the Bloch sphere. The Bloch vector adiabatically follows the driving vector \vec{D} rotation provided that the Bloch vector precession period around \vec{D} , $2\pi/\Omega$, is much smaller than the driving vector flipping time Ω/r [13]. This condition reads as:

$$r \ll \frac{\Omega^2}{2\pi}. \quad (9)$$

Then the Bloch vector follows \vec{D} adiabatically from downward to upward orientation on the Bloch sphere, which corresponds to the atomic state swapping. An additional condition arises because the Bloch vector rotation is a coherent process that must take place on a time interval much smaller than the coherences lifetime T_2 . This condition is expressed as:

$$\pi\Omega\gamma_{12} \ll r \quad (10)$$

where $\gamma_{12} = (\pi T_2)^{-1}$.

The infinite duration condition can be replaced by a more tractable requirement. Let the excitation field shine the atom for a finite time interval. Illumination starts at time t_i with detuning $\Delta + \dot{\varphi}(t_i)$ from resonance. After crossing the resonance, the laser is switched off at time t_f , at distance $\Delta + \dot{\varphi}(t_f)$ from the atomic frequency. The process can be described as an adiabatic transfer provided the laser is switched on and off at detuning from resonance much larger than the Rabi frequency. For positive chirp rate this condition reads as:

$$\begin{aligned} \Delta + \dot{\varphi}(t_i) &\ll -\Omega, \\ \Delta + \dot{\varphi}(t_f) &\gg \Omega. \end{aligned} \quad (11)$$

The shape of this finite duration chirped pulse is represented in Figure 1a.

We aim at swapping states over a narrow spectral interval, the atomic frequency distribution covering a broad inhomogeneous width. In other words, we want to selectively address atoms embedded in a broad absorption line. The adiabatic process we described above does not accomplish such a selective excitation. If we try to excite a spectral interval Δ_0 using a fixed amplitude, frequency swept field with duration Δ_0/r , the finite duration condition (11) is not satisfied at the edges of the swept interval. As a result, the level population difference is affected outside the laser sweeping range, exhibits oscillations all over the excited interval and does not show steep slopes at the edges of the selected region [14].

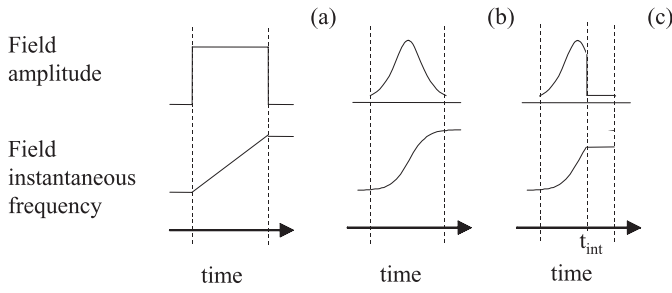


Fig. 1. Driving field amplitude and frequency variation for a finite duration, constant amplitude, linearly frequency chirped pulse (a), a complex hyperbolic secant (CHS) pulse (b), and an interrupted CHS pulse (c), where the CHS amplitude and frequency variations are switched off at time t_{int} .

3 Frequency selective adiabatic passage with complex hyperbolic secant pulses

Complex Hyperbolic Secant (CHS) pulses appear to offer an appropriate tool to achieve frequency selective excitation within an inhomogeneously broadened absorption line. CHS excitation was first considered in the search for analytic solutions to the Bloch equations [15–17]. In the frame of NMR [8], it was proved that CHS pulses have potential to create total spin inversion over a sharply defined region within an inhomogeneously broadened spectrum. With this excitation mode, more than half ground state population was excited to upper level in Rb gases using femtosecond light pulses [9, 10]. Recently, in the framework of quantum computing in rare-earth ions doped crystals, CHS pulses were proposed by Roos and Mølmer as a tool to efficiently swap states in a two-state system, and to optically pump a three-level system in a dark state [18].

3.1 Infinite duration CHS without relaxation: the adiabatic condition

The complex field amplitude $\mathcal{E}(t)e^{i\varphi(t)}$ of a CHS pulse is defined as

$$\mathcal{E}(t)e^{i\varphi(t)} = \mathcal{E}(t_0)\{\text{sech}[\beta(t - t_0)]\}^{1-i\mu} \quad (12)$$

where μ is a real constant and β is related to the pulse width. The corresponding Rabi frequency and instantaneous laser frequency are given by:

$$\begin{aligned} \Omega(t) &= \Omega_0 \text{sech}[\beta(t - t_0)] \\ \nu(t) &= \nu_0 + \frac{\mu\beta \tanh[\beta(t - t_0)]}{2\pi}. \end{aligned} \quad (13)$$

The variation of the amplitude and of the frequency around ν_0 is represented in Figure 1b.

An adiabatic condition similar to (9) shall be satisfied so that state swapping proceeds efficiently under CHS excitation. According to reference [8], state swapping is achieved over a rectangular shaped spectral interval with such pulses when $\mu > 2$ and $\Omega_0 > \beta\mu$. Although

calculation is restricted to $\Omega_0 > \beta\mu$ in reference [8], investigation can be extended to the $\Omega_0 < \beta\mu$ region. When $\Omega_0 < \beta\mu$, the final level population difference can be calculated as:

$$\begin{aligned} w_{t \rightarrow +\infty} &= -\tanh \pi \left(\frac{\Delta}{2\beta} + \frac{\mu}{2} \right) \tanh \pi \left(\frac{\Delta}{2\beta} - \frac{\mu}{2} \right) \\ &\quad - \cosh(\pi q) \text{sech} \left[\pi \left(\frac{\Delta}{2\beta} + \frac{\mu}{2} \right) \right] \text{sech} \left[\pi \left(\frac{\Delta}{2\beta} - \frac{\mu}{2} \right) \right] \end{aligned} \quad (14)$$

where $q = \sqrt{\mu^2 - \Omega_0^2/\beta^2}$. This expression is very similar to the $\Omega_0 > \beta\mu$ expression derived in reference [8], except $\cos[\pi\sqrt{\Omega_0^2/\beta^2 - \mu^2}]$ has been replaced by $\cosh(\pi q)$. Total population transfer is achieved over the spectral interval $-\beta\mu < \Delta < \beta\mu$ provided the second term on the right hand side of equation (14) is much smaller than unity. As in the case $\Omega_0 > \beta\mu$, the swapped spectral region is defined more sharply as μ increases [8]. If $\mu > 2$, the second term reduces to $\cosh(\pi q) \exp(-\pi\mu)$. This quantity is much smaller than unity if $\pi q \ll 1$. When $\pi q > 1$, the expression can be rearranged as:

$$\begin{aligned} \cosh(\pi q) \exp(-\pi\mu) &\approx \frac{1}{2} \exp[\pi(q - \mu)] \\ &= \frac{1}{2} \exp \left[-\frac{\mu\pi a^2}{1 + [1 - a^2]^{1/2}} \right] \end{aligned} \quad (15)$$

where $a = \Omega_0/\mu\beta$. This is much smaller than unity if:

$$\frac{\mu\pi}{2} a^2 \gg 1. \quad (16)$$

The chirp rate reads as:

$$r(t) = \frac{d\nu}{dt} = \frac{\mu\beta^2}{2\pi} \frac{1}{\cosh^2[\beta(t - t_0)]}. \quad (17)$$

Therefore, the condition (16) reduces to:

$$r_0 \ll \frac{\Omega_0^2}{4} \quad (18)$$

where $r_0 = r(t_0)$ and $\Omega_0 = \Omega(t_0)$. This is nothing but the adiabatic condition (9) at time $t = t_0$. Thus efficient population transfer can be achieved over the spectral interval $-\beta\mu < \Delta < \beta\mu$ provided $\mu > 2$ and the adiabatic condition is satisfied at $t = t_0$. Actually, given $\Omega(t)$ and $r(t)$ definitions (13, 17), the ratio $\Omega(t)^2/r(t)$ is constant and equals Ω_0^2/r_0 so that the adiabatic condition is satisfied at any moment, once satisfied at $t = t_0$. The condition (18) can be rewritten as:

$$\Omega_0 > 2\mu\beta/\sqrt{2\pi\mu} \quad (19)$$

which means that the maximum Rabi frequency need not be larger than the excited interval $2\mu\beta$. Actually efficient transfer can be accomplished with significantly smaller Rabi frequency provided $\mu \gg 1$.

Having related the transfer efficiency to the adiabatic condition, we can get insight into the physics of CHS excitation. As in the infinite duration linear chirp process,

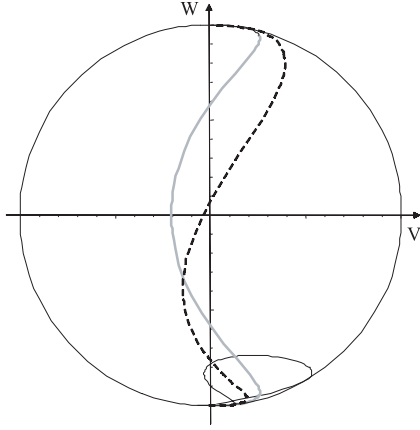


Fig. 2. Analytical calculation of the Bloch vector evolution interacting with an infinite duration CHS pulse. The Bloch vector head trajectory is reproduced in the v - w plane for the groups of ions respectively located at $\Delta = (3/2)\mu\beta$ (solid black line), $\Delta = (1/2)\mu\beta$ (solid thick grey line), and $\Delta = 0$ (dashed line). The laser is swept from $\Delta = \mu\beta$ to $\Delta = -\mu\beta$. The parameters of the calculation are $\mu = 30$ and $\Omega_0/\mu\beta = 2/3$.

we consider that the Bloch vector follows the driving vector. Therefore, to describe the Bloch vector evolution, we just need examine the driving vector motion.

Depending whether the atomic detuning Δ stays within or outside the spectral interval $[-\beta\mu, \beta\mu]$, the vector $\vec{D}(\Omega, 0, \Delta + \dot{\varphi}(t))$ flips from downward to upward orientation or remains within the same half-space. If $\Delta < -\beta\mu$ (respectively $\Delta > \beta\mu$), \vec{D} remains downward (respectively upward) oriented. We identify the Bloch vector with a unit vector aligned along \vec{D} . We must take care of the downward initial orientation of Bloch vector. Hence:

$$\vec{B} = \text{sign}(\beta\mu - \Delta)\vec{D}/\sqrt{\Omega^2 + (\Delta + \dot{\varphi})^2}. \quad (20)$$

Since \vec{D} has no component along Ov , the Bloch vector horizontal component v vanishes. Thus according to equations (4, 5), the level population difference and the off diagonal matrix element reads as:

$$\begin{aligned} \rho_{12} &= \text{sign}(\beta\mu - \Delta)\frac{1}{2}\frac{\Omega}{\sqrt{\Omega^2 + (\Delta + \dot{\varphi})^2}}e^{2i\pi\nu_0(t-t_0)+i\varphi(t)} \\ n_{12} &= \text{sign}(\beta\mu - \Delta)\frac{\Delta + \dot{\varphi}}{\sqrt{\Omega^2 + (\Delta + \dot{\varphi})^2}}. \end{aligned} \quad (21)$$

It appears that, outside the swept interval, the Bloch vector vertical component departs from -1 , the maximum variation reaching $1 - [\sqrt{\Delta^2 - \beta^2\mu^2}/\sqrt{\Omega_0^2 + \Delta^2 - \beta^2\mu^2}]$. This corresponds to a maximum horizontal component length of $\Omega_0/\sqrt{\Omega_0^2 + \Delta^2 - \beta^2\mu^2}$. For a given value of Ω_0 , the maximal population difference approaches 0 the closer as $|\Delta| - \beta\mu$ is smaller than Ω_0 . Then the vertical component returns to -1 as time elapses (Fig. 2).

3.2 Influence of coherence relaxation

We have neglected relaxation so far. Population decay can often be ignored, but we have to take account of the finite

coherence lifetime T_2 . During the flipping time from downward to upward orientation, the Bloch vector exhibits horizontal components, that represent the coherence of states $|1\rangle$ and $|2\rangle$. These components decrease with a decay rate $1/T_2 = \pi\gamma_{12}$. Thus, during the flipping time, the Bloch vector length decreases as:

$$\frac{d|B|^2}{dt} = -2\pi\gamma_{12}|B_h(t)|^2 \quad (22)$$

where $B_h = \sqrt{u^2 + v^2}$ is the horizontal component module. When the Bloch vector gets its final vertical position, its length is smaller than unity. The level population difference variation is given by:

$$\begin{aligned} w^2(+\infty) - w^2(-\infty) &= B^2(+\infty) - B^2(-\infty) \\ &= -2\pi\gamma_{12} \int_{-\infty}^{+\infty} |B_h(t)|^2 dt \end{aligned} \quad (23)$$

provided $\gamma_{12} \int_{-\infty}^{+\infty} |B_h(t)|^2 dt \ll 1$. In the adiabatic regime, the horizontal projection of the Bloch vector reads as:

$$\begin{aligned} |B_h(t)|^2 &= \frac{\Omega^2(t)}{\Omega^2(t) + (\Delta + \dot{\varphi}(t))^2} \\ &= \frac{\Omega_0^2}{\Omega_0^2 + [\Delta \cosh(\beta(t-t_0)) + \mu\beta \sinh(\beta(t-t_0))]^2}. \end{aligned} \quad (24)$$

The integral $\int_{-\infty}^{+\infty} |B_h^2(t)|$ is calculated as:

$$\begin{aligned} \int_{-\infty}^{+\infty} |B_h^2(t)| dt &= \frac{a}{\beta\sqrt{-1+a^2+x^2}} \\ &\times \ln \left\{ \frac{(a + \sqrt{-1+a^2+x^2})^2}{|x^2-1|} \right\} \end{aligned} \quad (25)$$

where $a = \Omega_0/\mu\beta$ and $x = \Delta/\mu\beta$. At $a = 1$ and $\Delta = 0$, the integral reduces to $2/\beta$. Thus we get:

$$n_2(+\infty) = 1 - \pi\frac{\gamma_{12}}{\beta}. \quad (26)$$

Hence, to be efficient, a CHS population transfer must satisfy the condition:

$$\pi\Omega_0\gamma_{12} \ll r_0 \quad (27)$$

which coincides with the corresponding condition for infinite duration, linear chirp excitation.

We noticed above that outside the selected spectral window, the Bloch vector rotates under the action of the driving field and ultimately returns to its initial position. The finite coherence lifetime prevents the Bloch vector from exactly recovering its initial position. This is illustrated in Figure 3, where we compare the wings of the

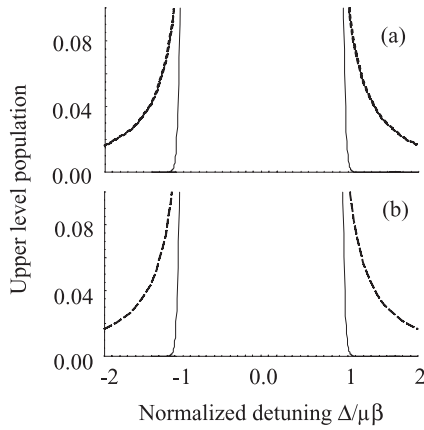


Fig. 3. Upper level population spectral distribution wings in the presence (dashed line) and the absence (solid line) of relaxation, with $T_2 = 8\beta^{-1}$, according to the numerical calculation (a) and the adiabatic model (b). The parameters of the calculation are $\mu = 30$, $\Omega_0/\mu\beta = 2/3$.

upper level population spectral distribution in the presence and in the absence of relaxation. In the wings, the adiabatic approximation expression of the upper level population reads as:

$$n_2(+\infty) = \frac{\pi \gamma_{12}}{2 \beta} \frac{a}{\sqrt{-1 + a^2 + x^2}} \times \ln \left\{ \frac{(a + \sqrt{-1 + a^2 + x^2})^2}{|x^2 - 1|} \right\}. \quad (28)$$

This analytic expression coincides with the numerical calculation result as illustrated in Figure 3.

3.3 Finite duration pulses

Experimentally, excitation is provided by finite duration pulses. Then, the driving vector is not exactly aligned along the vertical axis when the field is switched on. The geometrical model can be extended to this situation. The Bloch vector $\vec{B} = (u, v, w)$ precesses around $\vec{D} = (\Omega, 0, \Delta + \dot{\varphi})$. With the help of the rotation:

$$R(t) = \begin{pmatrix} \cos \theta & 0 & -\sin \theta \\ 0 & 1 & 0 \\ \sin \theta & 0 & \cos \theta \end{pmatrix} \quad (29)$$

where $\cos \theta = (\Delta + \dot{\varphi})/\sqrt{\Omega^2 + (\Delta + \dot{\varphi})^2}$, $\sin \theta = \Omega/\sqrt{\Omega^2 + (\Delta + \dot{\varphi})^2}$ the driving field coordinates are changed into $[D'] = R[D] = (0, 0, \sqrt{\Omega^2 + (\Delta + \dot{\varphi})^2})$. Let the field be switched on at time t_i . At t_i the Bloch vector coordinates can be expressed in the rotating frame as:

$$[B'] = R[B] = (\sin \theta_i, 0, -\cos \theta_i) \quad (30)$$

where $\theta_i = \theta(t_i)$. We assume the Bloch vector adiabatically follows the driving vector, around which it precesses

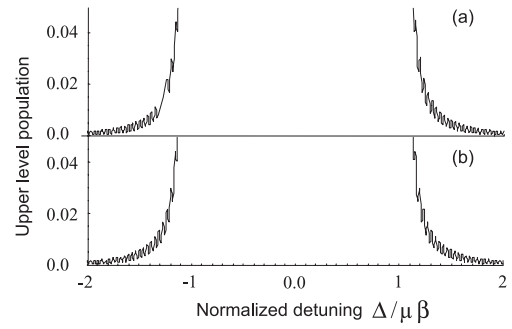


Fig. 4. Upper level population spectral distribution wings after a $6\beta^{-1}$ duration CHS pulse, in the absence of relaxation, according to the numerical calculation (a) and the adiabatic model (b). The parameters of the calculation are $\mu = 30$ and $\Omega_0/\mu\beta = 2/3$.

at frequency $-\sqrt{\Omega^2 + (\Delta + \dot{\varphi})^2}$. At time t , the Bloch vector coordinates in the rotating frame turn out to be:

$$[B'(t)] = (\sin \theta_i \cos \Phi, -\sin \theta_i \sin \Phi, -\cos \theta_i) \quad (31)$$

where $\Phi = \int_{t_i}^t \sqrt{\Omega(t')^2 + [\Delta + \dot{\varphi}(t')]^2} dt'$. The original frame Bloch vector coordinates are recovered with the help of $[B(t)] = R^{-1}(t)[B'(t)]$. Therefore at time t the components u, v, w read as:

$$\begin{cases} u = \sin \theta_i \cos \theta \cos \Phi - \cos \theta_i \sin \theta \\ v = -\sin \theta_i \sin \Phi \\ w = -\sin \theta_i \sin \theta \cos \Phi - \cos \theta_i \cos \theta \end{cases}. \quad (32)$$

Let us consider a time symmetric pulse of duration $2T \gg \beta^{-1}$. Then expansion of equation (32) leads to the following expression of upper level population $n_2(\Delta)$ in the outer wings of the selected window:

$$n_2(\Delta) = \frac{\Omega^2(T)}{2(\Delta^2 - \mu^2\beta^2)} \left[\frac{2\mu^2\beta^2}{\Delta^2 - \mu^2\beta^2} + 1 - \cos \phi \right] \quad (33)$$

when $0 < \Delta^2 - \mu^2\beta^2 \ll \mu^2\beta^2$, the oscillatory term is negligible and the population exhibits a hyperbolic dependence on the distance from the window edge. The $1 - \cos \phi$ dependence is dominant when $\Delta^2 \gg 2\mu^2\beta^2$. These features are illustrated in Figure 4, where the wings of the calculated upper level population spectral distribution are displayed under finite duration CHS conditions. The geometrical model shows an excellent agreement with the numerical calculation.

In conclusion, both coherence decay and finite pulse duration can deteriorate the CHS excitation spectral selectivity. The total duration of the CHS pulse in terms of β^{-1} should be adjusted in such a way that limited excitation time be less harmful to spectral selectivity than the coherence decay. In the next sections, we present an experiment that we devised to explore various aspects of CHS excitation. Specifically, we have examined the population transfer efficiency and the temporal evolution of the Bloch vector.

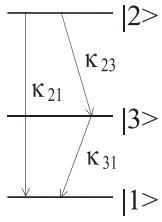


Fig. 5. Level scheme of $\text{Tm}^{3+}:\text{YAG}$. The optical excitation is tuned to transition $|1\rangle \rightarrow |2\rangle$. The upper level $|2\rangle$ mainly decays to the shelving state $|3\rangle$ through non-radiative relaxation. The decay rates connecting the levels are denoted as κ_{ij} .

4 Experimental investigation of population transfer

Experimental investigation is performed in a 0.1 at.% $\text{Tm}^{3+}:\text{YAG}$ sample, cooled at 1.4 K in a liquid helium bath cryostat. The crystal, grown at Scientific Materials Corp., is cut and polished normally to $[1\bar{1}0]$ direction. The crystal is 2 mm thick along the light propagation direction $[1\bar{1}0]$, which corresponds to an optical density ~ 0.1 . The Tm^{3+} ions occupy six crystallographically equivalent but orientationally inequivalent sites with dodecahedral point symmetry D_2 . We polarize the incident beams along direction $[001]$. Then four sites undergo identical interaction with the field. The two remaining sites are not coupled with the field, which is orthogonal to their interaction dipole moment [20].

The level scheme of $\text{Tm}^{3+}:\text{YAG}$ ions is illustrated in Figure 5. CHS excitation is applied to the optical transition at 793 nm between the ground state $|1\rangle$ and the excited state $|2\rangle$. The excited state decays to the shelving state $|3\rangle$ with a branching ratio close to 0.75, that we measured by photon echo techniques. The shelving state decay rate κ_{31} ($\kappa_{31}^{-1} \sim 10$ ms) is much smaller than the upper level decay rate $\kappa_{21} + \kappa_{23}$ ($(\kappa_{21} + \kappa_{23})^{-1} \sim 0.5$ ms). We also measured those decay rates with photon echo experiments.

As the optical density is proportional to the population difference $n_1 - n_2$, we probe the transfer efficiency by measuring the transmission of an attenuated probe laser beam through the exposed sample. The experimental set-up is represented in Figure 6. The 793 nm extended cavity diode laser is closed by a diffraction grating in Littrow configuration. Pound-Drever-Hall procedure is used to lock the laser to a high finesse (~ 3000), 10 cm-long Fabry-Perot interferometer. An intracavity electro-optic crystal closes the locking loop. Relative stability of 250 Hz has been achieved on 10 ms timescale [12]. After spatial filtering in an optical fiber, the beam is then amplitude and phase shaped by an acousto-optic modulator (AO_1). A high frequency waveform generator (Sony-Tektronix AWG 520) synthesizes the 80 MHz radio-frequency carrier used to drive the acousto-optic modulator AO_1 through a RF amplifier. This enables us to directly shape the beam in phase and amplitude with the AWG520 clock precision of 1 gigasample/s and a 10 bits amplitude dynamic range. This situation is contrasted with previous experimental investigations in the femtosecond range, where optical techniques were used to indirectly shape the laser beam [11]. The driving power of the modulator is adjusted in such a way that AO_1 operates in the linear regime, i.e. the transmitted field is proportional to the driving voltage. The spot waist at $1/e^2$ on the modulator is $w_0 = 175 \mu\text{m}$. The modulator is imaged on the crystal in such a way that the illuminated region does not move when the laser is frequency swept by the modulator. The spot waist at $1/e^2$ on the crystal is $w_1 = 33 \mu\text{m}$. The laser power at the cryostat input is $P_1 \sim 0.6$ mW. According to the transition dipole moment value reported in reference [19], this corresponds to a maximum Rabi frequency $\Omega_0 \sim 2.0 \times 10^6 \text{ s}^{-1}$ and to a ratio $\Omega_0^2/r_0 \sim 22.0$ for a frequency sweep of 750 kHz during $75 \mu\text{s}$ ($\beta = 0.08 \mu\text{s}^{-1}$, $\mu \sim 30$). The crystal is then

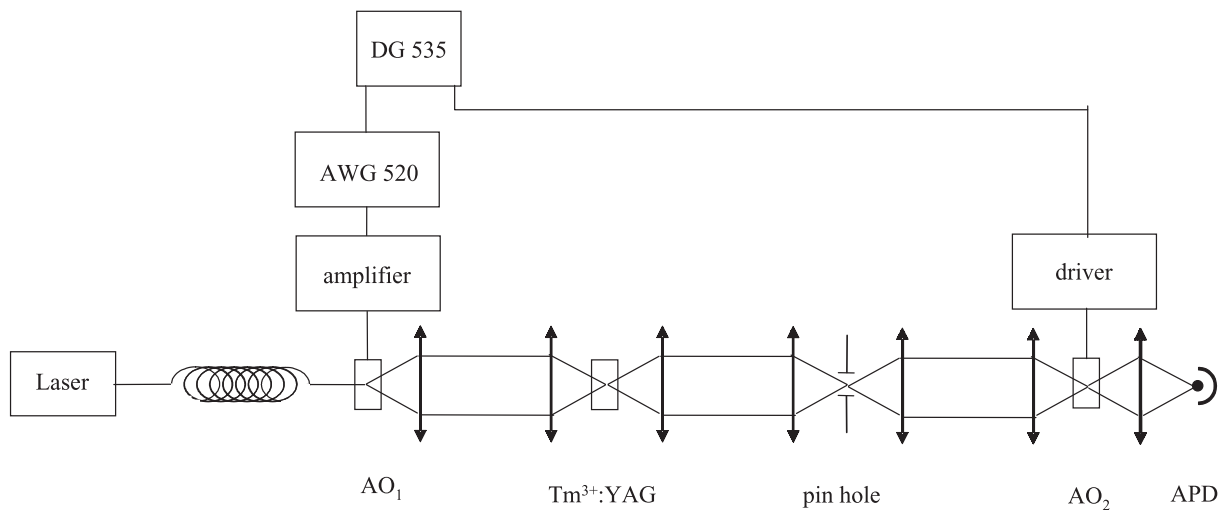


Fig. 6. Experimental set-up. The laser beam is spatially filtered by an optical fiber. The CHS pulse is shaped by the acousto-optic modulator AO_1 that is directly fed at 100 MHz RF carrier frequency by a 1 Gs/s arbitrary wave form generator (Sony-Tektronix AWG 520). AO_1 is imaged on the sample, which is cooled down to 1.5 K by cryogenic techniques. The crystal is imaged on a pinhole that selects the central part of the illuminated spot. AO_2 protects the detector from the excitation pulses. The time sequence is controlled by the pulse generator (DG 535).

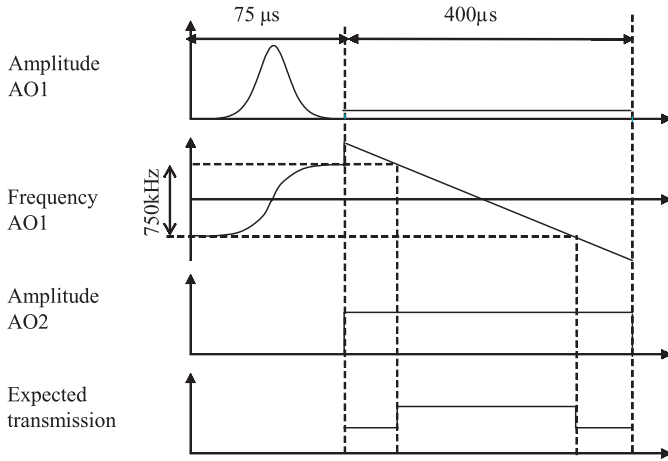


Fig. 7. Time diagram of an excitation/probing sequence for an adiabatic transfer experiment using a CHS pulse. During the excitation step, the laser field amplitude and phase are CHS shaped by AO₁, while AO₂ is closed. During the probing step, the laser beam is attenuated and the frequency is linearly swept by AO₁ over the excited region. AO₂ is open. One expects probe beam amplification over the interval where ground state population has been transferred to the upper level.

imaged on a $100 \mu\text{m}$ diameter pinhole, so that only the central region of the exposed region is probed. The spot diameter at $1/e^2$ on the pinhole is $2w_2 = 260 \mu\text{m}$. The transmitted beam is detected on an avalanche photodiode (Hamamatsu C5460), with a bandwidth of 10 MHz. The photodiode is protected from the excitation pulse by the acousto-optic modulator AO₂. A pulse generator (Stanford Research DG 535) drives AO₂ and triggers the AWG 520 generator.

The time diagram for an excitation/probing sequence is presented in Figure 7. At the excitation stage, AO₁ shapes the CHS pulse while AO₂ is closed to protect the detector. The laser frequency is scanned over 750 kHz during $\tau = 75 \mu\text{s} = 6\beta^{-1}$, which corresponds to $\mu = 29.45$ and to a variation of $\beta(t - t_0)$ from -3 to $+3$. The field amplitude on the pulse edges is $<1/10$ its maximum value. At the read-out stage, the probing beam is strongly attenuated by AO₁ while AO₂ is opened. In the probing stage, we scan the laser over a frequency interval twice as large as the excited domain. This way, we also probe unexposed ions. The chirp rate is reduced to $r_p = 3.75 \times 10^9 \text{ Hz/s}$ so that the read-out spectral resolution, given by $\sqrt{r_p}$, is $\sim 60 \text{ kHz}$. One expects amplification of the probe beam over the frequency interval excited by the CHS pulse.

The quantity of interest, the optical density D , can be expressed in terms of the transmitted intensity as:

$$D = \log \left(\frac{I_0}{I} \right) \quad (34)$$

where I_0 and I respectively represent the incident and transmitted intensity. The optical density is proportional to the level population difference $n_1 - n_2$. All the ions are supposed to be in the ground state before excitation and this initial ground state population is normalized to

unity. Let $D^{(0)}$ and $D^{(1)}(t)$ respectively represent the optical density before excitation and at time t after excitation. The density ratio reads as

$$\frac{D^{(1)}(t)}{D^{(0)}} = n_1(t) - n_2(t). \quad (35)$$

Immediately after excitation, all the population is shared between levels 1 and 2, so that

$$n_1(0) + n_2(0) = 1. \quad (36)$$

We assume that the upper level population exponentially decays at rate $\kappa = \kappa_{21} + \kappa_{23} = 2000 \text{ s}^{-1}$ with branching ratios to shelving and ground states respectively given by $\eta = 0.75$ and $1 - \eta$. Therefore $D^{(1)}(t)$ can be expressed in terms of $n_2(0)$ only as

$$\frac{D^{(1)}(t)}{D^{(0)}} = 1 - n_2(0)(\eta + (2 - \eta) \exp(-\kappa t)). \quad (37)$$

Finally, from equations (34) and (37), one derives the expression of $n_2(0)$:

$$n_2(0) = \frac{1}{n + (2 - \eta) \exp(-\kappa t)} \frac{\log(I_{TP}(t)/I_{TU})}{\log(I_0/I_{TU})} \quad (38)$$

where I_{TU} and I_{TP} respectively represent the transmitted intensity through the unexposed and excited sample. The intensity I_{TU} is obtained in the far wings of the transmission profile, outside the exposed region. The amplified intensity I_{TP} is obtained in a single shot regime, where the experiment 10 Hz repetition rate is ~ 10 times smaller than the shelving state decay rate. The incident intensity I_0 coincides with the transmitted intensity through the totally bleached crystal. This is measured in the accumulation regime where the excitation/probing sequence is repeated at a rate of 2 KHz. The excited ions are pumped to the shelving state due to the repetition of the excitation, and the transition is completely bleached.

The resulting upper level population spectral distribution is displayed in Figure 8 together with the computed profile. Numerical calculation was performed with $\Omega_0 = 1.6 \times 10^6 \text{ s}^{-1}$ and $T_2 = 100 \mu\text{s}$. The experimental transfer rate reaches $\sim 94\%$, slightly larger than the computed value. Accuracy is mainly limited by the optical density measurement precision. The resulting error on $n_2(0)$ is estimated to be $\sim 3\%$. The transmission profile after accumulated excitation was used to calibrate the incident intensity. This profile also provides information on frequency selectivity. Actually, the sample exposed to accumulated excitation appears to be totally bleached outside the excitation window. This is a signature of wing excitation associated with finite coherence lifetime, as discussed in Section 3. In accordance with theoretical predictions, CHS excitation appears to offer a good way for efficient quantum state swapping in a macroscopic inhomogeneously broadened ion ensemble. Spectral selectivity requires that the pulse duration be much smaller than the coherence lifetime, a condition that is not totally satisfied in the present experiment.

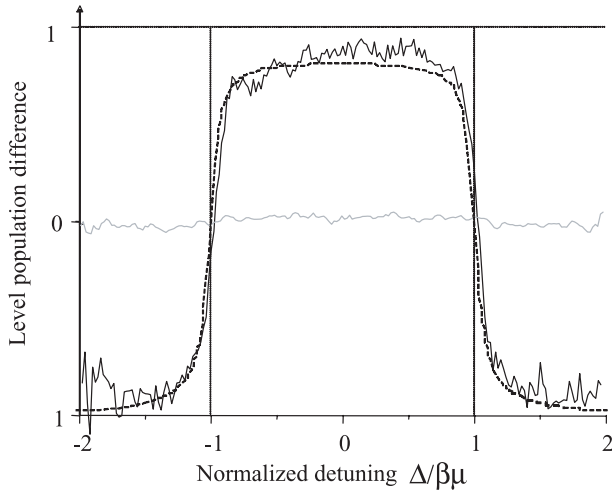


Fig. 8. Calculated (dashed line) and measured (solid black line) upper level population spectral distribution versus normalized detuning just after excitation by a CHS pulse of duration $6\beta^{-1}$. The parameters of the CHS excitation are $\mu = 30$, $\beta = 0.08 \mu\text{s}^{-1}$ and $\Omega_0/\mu\beta = 0.9$. The coherence lifetime is $T_2 = 8\beta^{-1}$. The solid grey line represents the accumulation regime with an excitation repetition rate of 2 kHz.

Information derived in this experiment is not limited to the level population difference. As shown in the next section, we are able to get more detailed knowledge on the Bloch vector motion, including the atomic coherence component evolution.

5 Bloch vector motion as expressed by free induction decay

The Bloch vector exhibits horizontal components during the flipping time. If the excitation field is interrupted at time t_{int} , the coherences evolve freely and can be expressed at time t as:

$$\rho_{12}(\nu_{12}, t) = \rho_{12}(\nu_{12}, t_{int})e^{2i\pi\nu_{12}(t-t_{int})}. \quad (39)$$

These oscillating coherences emit a Free Induction Decay (FID) signal [15] that reflects the atomic superposition state at t_{int} . The FID signal amplitude $E_{FID}(t) = \mathcal{E}_{FID}(t)e^{2i\pi\nu_0 t + i\varphi(t)} + cc$ is proportional to the sum of the different atoms contributions. At time $t > t_{int}$, it reads as:

$$\begin{aligned} \mathcal{E}_{FID}(t) &= -in_0 \frac{kd_{ab}L}{2\varepsilon_0} e^{-2i\pi\nu_0(t-t_0)} \int \rho_{12}(\nu_{12}, t) d\nu_{12} \\ &= \frac{kd_{ab}L}{2\varepsilon_0} e^{i[\varphi(t_{int}) - \frac{\pi}{2}]} \int \tilde{\rho}_{12}(\Delta, t_{int}) e^{-2i\pi\Delta(t-t_{int})} d\Delta \end{aligned} \quad (40)$$

where n_0 , k , and L respectively represent the active center density, the wave vector and the sample length. This expression is proportional to the Fourier transform of the coherence spectral distribution at time t_{int} , $F = \int \tilde{\rho}_{12}(\Delta, t_{int}) e^{-2i\pi\Delta(t-t_{int})} d\Delta$. This way, by interrupting

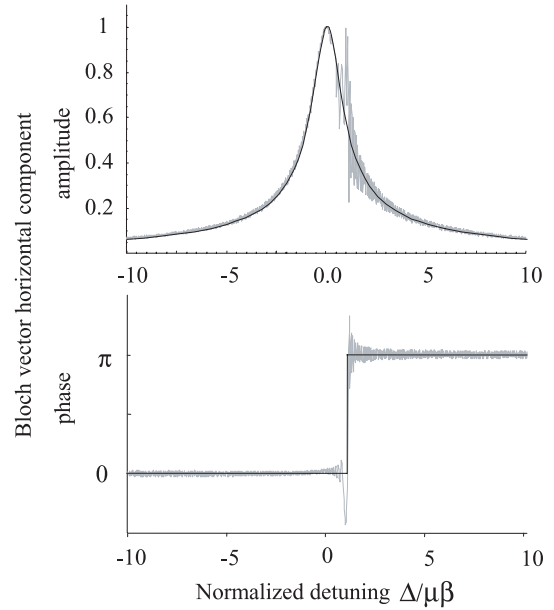


Fig. 9. Spectral distribution of the computed amplitude (a) and phase (b) of the Bloch vector horizontal component after interruption of CHS excitation at $t_{int} = t_0$. Computation has been performed with $\Omega_0 = 2\beta\mu/3$ and $\mu = 30$. The adiabatic model and the numerical solution of Bloch equation are respectively represented by solid black line and thick grey line.

the CHS excitation at different moments (Fig. 1c), we are able to derive information on the Bloch vector horizontal component all along the swapping state process.

Starting from zero when t_{int} equals the pulse switching time t_i , the FID signal amplitude grows as t_{int} is increased and should be maximal when the CHS pulse is interrupted at half-way ($t_{int} = t_0$). Indeed at this time the coherence spectral density is maximal. For an interruption time $t_{int} > t_0$, the amplitude of the FID signal decreases as a function of t_{int} , since the atomic coherences are then transformed into atomic populations by the CHS pulse. The signal should vanish when all the excited atoms are in the upper level.

We consider a finite duration time-symmetric CHS excitation and concentrate on the Bloch vector horizontal component investigation at two specific times, i.e. at mid pulse ($t_{int} = t_0$) and at the end of the pulse. Let us first examine atomic excitation at $t_{int} = t_0$. At that moment, the laser frequency has been scanned over the interval $\nu_0 - \mu\beta/2\pi < \nu < \nu_0$. The numerical calculation of the amplitude and phase of the horizontal component is displayed in Figure 9 corresponding to a total duration of $6\beta^{-1}$ and a Rabi frequency value $\Omega_0 = 2\mu\beta/3$ with $\mu = 30$. We have neglected the coherence decay. In the same figure, we reproduce the prediction of the geometric adiabatic model. In this model we assume that the Bloch vector is aligned along the driving vector, which corresponds to coupling starting at $t_i = -\infty$. The main features are correctly described by the simple model, some discrepancy being observed only at $\Delta \sim \mu\beta$. The excited atoms distribution exhibits a large width with extensive wings.

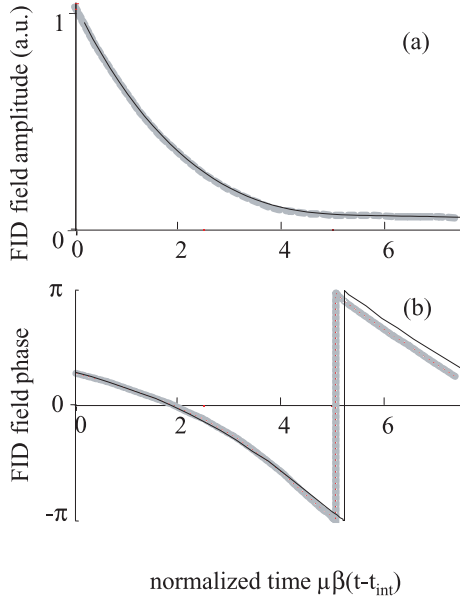


Fig. 10. Computed FID field amplitude (a) and phase (b) temporal evolution after interruption of CHS excitation at $t_{int} = t_0$. Computation has been performed with $\beta = 0.08 \mu\text{s}^{-1}$ and $\Omega_0 = 2\beta\mu/3$ with $\mu = 30$. The adiabatic model and the numerical solution of Bloch equation are respectively represented by solid black line and thick grey line.

In addition, although the laser resonantly interacted only with the atoms such that $\Delta > 0$, the length of the Bloch vector horizontal component distribution appears to be symmetric around $\Delta = 0$. The π phase discontinuity at $\Delta = \mu\beta$ corresponds to the sign change that appears in equation (20).

It appears that the mid-pulse interrupted CHS excitation might offer a way to prepare atoms in a specific superposition state. First one selects a narrow frequency group of atoms at a specific distance Δ from ν_0 , by pumping atoms with different absorption frequency outside of the spectral interval to an auxiliary state. Such a preparation has already been demonstrated in rare-earth ions embedded in crystals using hard pulses [20] or RAP techniques with chirped pulses [21]. Then one applies the mid-pulse interrupted CHS excitation to the selected group of atoms. The pulse leaves them oriented along the final \vec{D} direction:

$$\hat{D} = \left(\Omega_0 / \sqrt{\Omega_0^2 + \Delta^2}, 0, \Delta / \sqrt{\Omega_0^2 + \Delta^2} \right). \quad (41)$$

The FID field amplitude and phase time evolution corresponding to Figure 9 has been computed according to equation (40). The result of the calculation of $F = \int \tilde{\rho}_{12}(\Delta, t_{int}) e^{-2i\pi\Delta(t-t_{int})} d\Delta$ is reproduced in Figure 10. From the adiabatic model expression of the signal amplitude, the decay rate at $t = t_{int}$ is calculated as:

$$\frac{1}{|E_{FID}(t_{int})|} \frac{d|E_{FID}(t_{int})|}{dt} = - \frac{(\pi/2) \sqrt{\Omega_0^2 + \mu^2\beta^2}}{\left[\text{arcsinh}\left(\frac{\mu\beta}{\Omega_0}\right) \right]^2 + \left(\frac{\pi}{2}\right)^2} \quad (42)$$

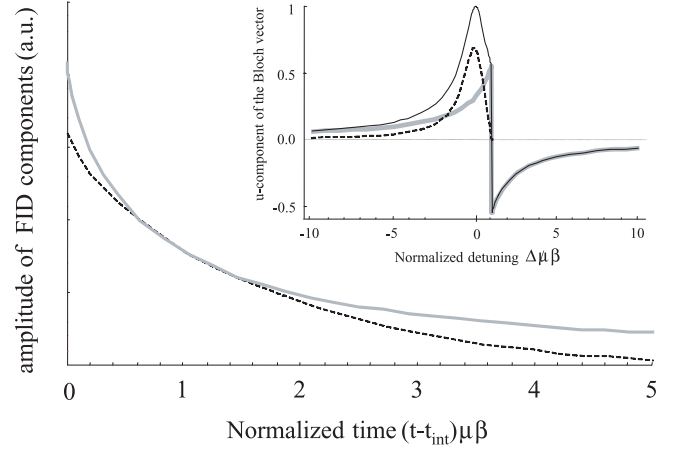


Fig. 11. In the inset: break down of the Bloch vector u -component distribution (solid line) as a sum of a dispersive contribution (grey solid line) and a complementary term (dashed line). The corresponding FID component time evolution is reproduced in the main frame. The dispersive contribution (grey solid line) dominates the complementary term (dashed line) at $(t - t_0)\mu\beta \gg 1$.

which is dominated by Ω_0 when $\Omega_0 \gg \mu\beta$. The continuous growing of the phase as a function of time reflects a frequency shift of the emission with respect to the central frequency ν_0 . The frequency shift at $t = t_{int}$ reads as:

$$\frac{1}{2\pi} \frac{d\varphi(t_{int})}{dt} = - \frac{1}{2\pi} \frac{\text{arcsinh}\left(\frac{\mu\beta}{\Omega_0}\right) \sqrt{\Omega_0^2 + \mu^2\beta^2}}{\left[\text{arcsinh}\left(\frac{\mu\beta}{\Omega_0}\right) \right]^2 + \left(\frac{\pi}{2}\right)^2}. \quad (43)$$

To get some insight into the underlying physics, we have broken down the Bloch vector u -component distribution as a sum of two terms (see the inset in Fig. 11). We build the first term as a dispersion profile by combining the hyperbolic branch observed at $\Delta \geq \mu\beta/2\pi$ with the branch obtained by inversion with respect to $\Delta = \mu\beta/2\pi$. Dispersion shape is typical of causal excitation by a monochromatic field at $\nu_0 - \mu\beta/2\pi$. Then we have to add a second term to complement the dispersive component and recover the Bloch vector u -component distribution. As shown in Figure 11, the additional term contribution to the FID signal decreases faster than the dispersive one as a function of time. Therefore, as time elapses, the FID signal is ultimately centered at $\nu_0 - \mu\beta/2\pi$.

We now consider the FID signal emitted at the end of the finite duration time-symmetric CHS pulse. The numerical calculation of the amplitude and phase of the horizontal component is displayed in Figure 12 corresponding to a total duration of $6\beta^{-1}$ and a Rabi frequency value $\Omega_0 = 2\mu\beta/3$ with $\mu = 30$. We have ignored the coherence decay. The prediction of the geometric adiabatic model is also shown in Figure 12a. To correctly describe the region $\Delta \sim \mu\beta$, we had to use the finite duration model instead of the model where the Bloch vector is aligned along the driving vector. This finite duration adiabatic model also predicts a phase distribution very close to the numerical calculation displayed in Figure 12b. In Figure 12a one

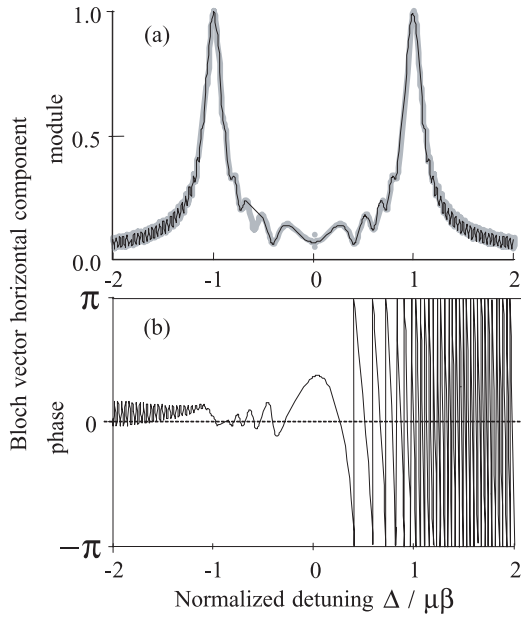


Fig. 12. Spectral distribution of the computed amplitude (a) and phase (b) of the Bloch vector horizontal component at the end of the finite duration time-symmetric CHS pulse. Computation has been performed with $\Omega_0 = 2\beta\mu/3$ and $\mu = 30$. The adiabatic model and the numerical solution of Bloch equation are respectively represented by solid black line and thick grey line.

can observe that the frequency areas with significant components are located at the edges of the excited window, where the transfer is not total and where some coherences survive. The main contributions to the FID signal should arise from these two wings according to equation (40). However, existence of coherences is not enough to have a FID signal emitted. In addition, those coherences have to oscillate in phase. Information of the phase distribution is provided by Figure 12b. This figure essentially reflects the inhomogeneous dephasing of the dipoles after they are built up.

Atoms located around $\Delta = \mu\beta$ are excited first, interacting resonantly with the field at time $\sim t_{int} - 4\beta^{-1}$. Their phase shift at time t is $\sim \Delta(t - t_{int} + 4\beta^{-1})$. Since, according to Figure 12a, the FWHM of their distribution at $\Delta = \mu\beta$ is $\sim 0.2\mu\beta$, their relative inhomogeneous dephasing is $\sim 0.1\mu\beta(t - t_{int} + 4\beta^{-1})$ and the corresponding emitted field amplitude varies as $\sim e^{-0.1\mu\beta(t - t_{int} + 4\beta^{-1})}$.

The situation is different for atoms located around $\Delta = -\mu\beta$. These atoms are still resonantly interacting with the driving field when the CHS pulse is switched off. Inhomogeneous dephasing is inhibited as long as interaction is maintained [23], as can be observed in Figure 12b. They start to dephase after the CHS is switched off. Therefore, their relative inhomogeneous dephasing at time t is $\sim 0.1\mu\beta(t - t_{int})$. Hence, one expects that their contribution to the emitted field be $\sim e^{0.4\mu} \sim 1.6 \times 10^5$ times larger than the contribution arising from atoms at $\Delta = \mu\beta$. In other words, no visible contribution is expected from atoms at $\Delta = \mu\beta$.

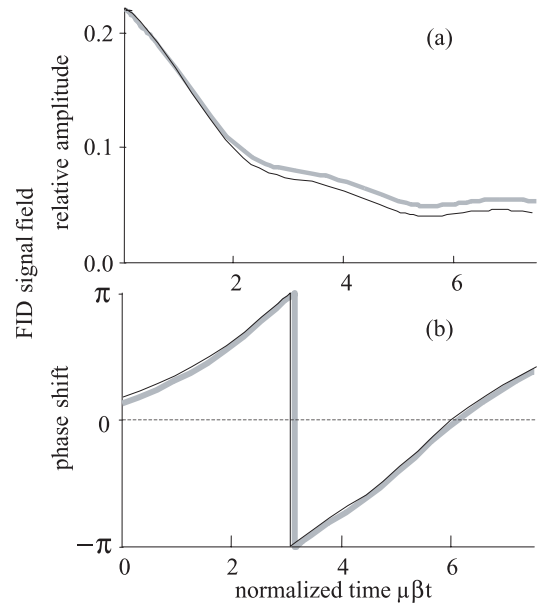


Fig. 13. Computed FID field amplitude (a) and phase (b) temporal evolution at the end of the finite duration time-symmetric CHS pulse. Computation has been performed with $\beta = 0.08 \mu\text{s}^{-1}$ and $\Omega_0 = 2\beta\mu/3$ with $\mu = 30$. The adiabatic model and the numerical solution of Bloch equation are respectively represented by solid black line and thick gray line.

The corresponding FID field amplitude and phase time evolution has been computed according to equation (40). The result of the calculation of $F = \int \tilde{\rho}_{12}(\Delta, t_{int}) e^{-2i\pi\Delta(t - t_{int})} d\Delta$ is presented in Figure 13. Surprisingly, the FID signal amplitude, as displayed in Figure 13a, exhibits a small beat structure that reflects the contribution of both $\Delta = \pm\mu\beta$ regions. The beat period is consistent with the $2\mu\beta$ frequency distance of these two regions. The signal amplitude is smaller than when observed after interruption of the CHS at mid-pulse. Indeed fewer atoms contribute to the signal. The decay rate is consistent with the spectral size of the radiating region. The FID signal phase shift with respect to the laser central frequency exhibits a quasi-linear time dependency, with a slope close to $\mu\beta$. Indeed the main contribution arises from atoms located at $\Delta \sim -\mu\beta$.

In the next section, we strive to experimentally demonstrate the various features discussed above.

6 Experimental free induction decay detection

In order to monitor the signal phase and to optimize the signal size, we use heterodyne detection. The time diagram of a FID experiment is presented in Figure 14. At the excitation stage, AO₁ is opened and shapes the CHS pulse while AO₂ is closed to protect the detector. The laser frequency is scanned until t_{int} according to the CHS profile. At that moment, the laser undergoes an abrupt frequency shift, 7 MHz above ν_0 and AO₁ transmission is strongly reduced. This provides us with the heterodyne reference that copropagates with the signal through the sample and

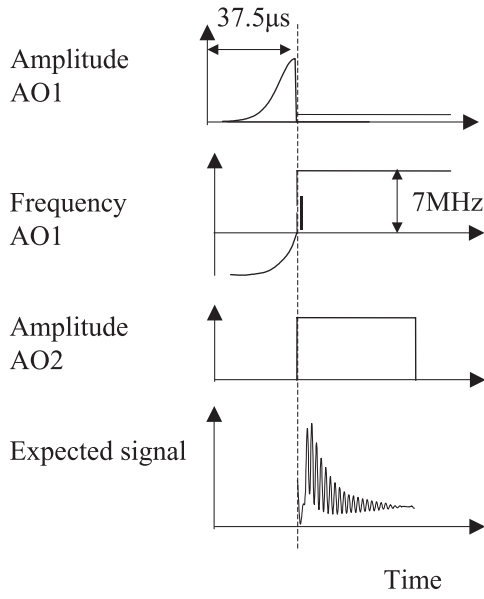


Fig. 14. Time diagram of an interrupted CHS pulse FID experiment with $\beta = 0.08 \mu\text{s}^{-1}$. During the exciting step, the laser field amplitude is shaped by AO₁. AO₂ is closed. During the detection stage, the laser field amplitude is attenuated and shifted of +7 MHz from the central frequency by AO₁ and AO₂ is open. The expected signal exhibits a beat between the laser beam and the FID signal.

is perfectly synchronized with the exciting field. The frequency shift value is limited by the detector bandwidth. The acousto-optic modulator AO₂ is opened for signal detection.

It should be pointed out that because of the acoustic wave propagation, excitation is not phase uniform within the sample. The laser beam phase φ in the modulator AO₁ is equal to:

$$\varphi(x, t) = 2\pi\nu_0 t + \varphi_{AO} \left(t - \frac{x}{v_{AO}} \right) \quad (44)$$

where x represents the coordinate along the propagation direction of the acoustic wave into the modulator, with $x = 0$ at the center of the spot, φ_{AO} represents the phase of the acoustic wave at position $x = 0$, and v_{AO} represents the propagation speed of the acoustic wave. To first order, φ reads as:

$$\begin{aligned} \varphi(x, t) &= 2\pi\nu_0 t + \varphi_{AO}(t) - \frac{x}{v_{AO}} \frac{d\varphi_{AO}}{dt} \\ &= 2\pi\nu_0 t + \varphi_{AO}(t) - 2\pi \frac{x}{v_{AO}} \nu_{AO}(t) \end{aligned} \quad (45)$$

where $\nu_{AO}(t)$ is the frequency of the acoustic wave. The 100 μm -diameter pinhole selects the 25 μm -diameter central part of the excited spot through 4-magnification-factor optics. This corresponds to a $d = 133 \mu\text{m}$ -diameter at the modulator. Therefore the phase difference of the observed region edges is:

$$\delta\varphi(t) = 2\pi \frac{d}{v_{AO}} \nu_{AO}(t). \quad (46)$$

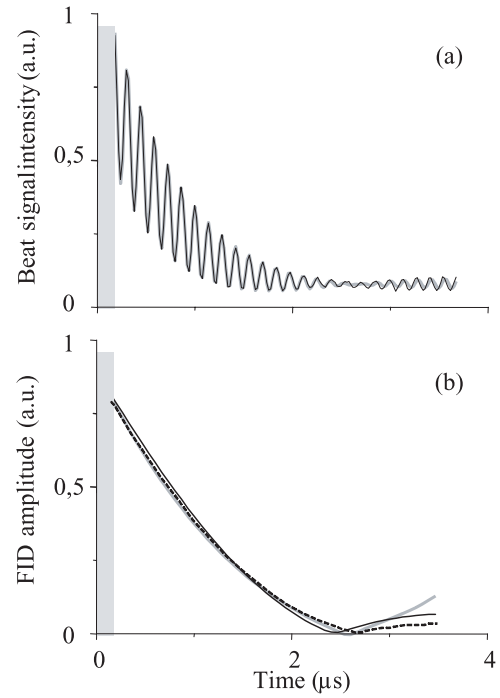


Fig. 15. Heterodyne detection ((a), black line) of the FID signal emitted after the mid-pulse interruption of a time symmetric CHS pulse of duration $6\beta^{-1}$. The FID signal ((b), grey line) is extracted by fitting the experimental data ((a), grey line) and is compared to the numerical calculation with $\Omega_0/\mu\beta = 0.3$ ((b), solid black line) and $\Omega_0/\mu\beta = 0.4$ ((b), dashed black line). The parameters of the CHS are $\mu = 30$ and $\beta = 0.08 \mu\text{s}^{-1}$. The coherence lifetime is $T_2 = 8\beta^{-1}$.

The phase difference vanishes at $t = t_0$. At the starting and the end of the CHS pulse, where $\nu_{AO}(t) = \pm\beta\nu/2\pi$, the phase difference reaches ~ 0.075 rad. This phase difference is small but may not be negligible. The phase non-uniformity is associated with an angular rotation of the incident beam wavevector. The 7 MHz frequency shift of the heterodyne reference beam induces a $\pi/2$ phase difference between the spot sides, which corresponds to a 10% reduction of beat contrast.

We first explore the Bloch vector at mid-CHS pulse by detecting the FID signal after interruption at $t_{int} = t_0$. The detected signal is presented in Figure 15a. Experimental conditions are $\beta = 0.08 \mu\text{s}^{-1}$, $\mu = 29.6$ and $T = 3\beta^{-1}$. The signal is unavailable during the ~ 60 ns rising time of the detector and the acousto-optic modulator AO₂.

To process the data, we fit the experimental signal intensity profile $I(t)$ with the following expression:

$$I(t) = S[G(t)]^2 + R + 2Q\sqrt{SR}G(t) \cos[f(t - t_{int}) + \Psi] \quad (47)$$

where S , R , f , G respectively represent the FID signal initial intensity, the heterodyning reference intensity, the beat frequency and the shape to be extracted. Ideally, the beat quality factor Q should equal unity. The fitted values lead to the profile displayed in grey in Figure 15. Factor Q turns out to be ~ 0.6 . We noticed above that the

reference beam is not exactly collinear with the signal, which slightly deteriorates the interference term. However, this is not enough to explain the small Q value. Geometry differences between the two beams might also affect this factor. The shape deduced from the fit is reproduced in Figure 15b. This shape matches a computed profile that corresponds to a Rabi frequency value significantly smaller than expected. Indeed, we measured $\Omega_0/\mu\beta = 0.9$ while the value deduced from the fit is located between $\Omega_0/\mu\beta = 0.3$ and $\Omega_0/\mu\beta = 0.4$. Precise positioning of the sample at beam waist is hampered by the cryostat. The observed discrepancy in Ω_0 value may result from wrong positioning. From the fit, we also obtain the phase at t_{int} and the frequency detuning. The measured phase of $F = \int \tilde{\rho}_{12}(\Delta, t_{int}) e^{-2i\pi\Delta(t-t_{int})} d\Delta$ at t_{int} is 3.01 rad, to be compared with the computed value of 0.69 rad. The initial phase measurement seems to be out of reach of our present set-up despite of the excellent wave control provided by AWG 520 generator. This may be ascribed to the blind zone that obscures the first 60 ns. If the signal phase shift were time-independent, the frequency parameter f should equal 7 MHz. Actually, this parameter turns out to equal 7.185 ± 0.005 MHz, which corresponds to an emission 185 ± 5 kHz down-shifted with respect to ν_0 . This is consistent with signal emission by the atoms located between $\nu_0 - \mu\beta/2\pi$ and ν_0 , as discussed in Section 5. In addition, this frequency shift is close to the computed shift of 179 kHz.

Then we investigate the Bloch vector distribution at the end of the excitation pulse by detecting the FID signal at $t_{int} = t_0 + T$. The experimental conditions are the same as in the previous experiment. The detected signal is displayed in Figure 16, together with the FID amplitude time evolution, extracted from the beat signal. The signal is scaled to the size of the signal obtained at mid-pulse. The experimental amplitude ratio of FID signals at $t_{int} = t_0$ and $t_{int} = t_0 + T$ is equal to 5.29, to be compared with the computed ratio of 5.16. The experimental time evolution of the FID signal amplitude (Fig. 16b) exhibits the expected beat structure with a beat period close to $(750 \text{ kHz})^{-1}$. The frequency detuning equals 6.70 ± 0.005 MHz, which corresponds to an emission 300 ± 5 kHz up-shifted with respect to ν_0 . This is consistent with signal emission by the atoms located around $\nu_0 + \mu\beta/2\pi$, as discussed in Section 5. The computed shift is ~ 375 kHz. As in the previous experiment, the measurement of initial phase is not meaningful because of the necessary extrapolation into the blind zone.

The experimental data nicely confirm the theoretical description presented in Section 5. However, the phase measurement does not lead to satisfactory results. This is a significant issue in experiments that aim at monitoring the atomic system quantum state.

7 Conclusion

We have applied a Rapid Adiabatic Passage approach to the analysis of CHS excitation, unlike some previous works that focused on CHS mathematical aspects [8, 22]. First we

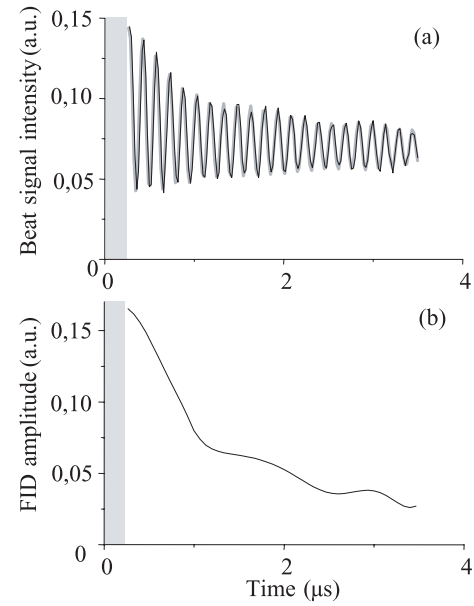


Fig. 16. Heterodyne detection ((a), black line) of the FID signal emitted after the time symmetric CHS pulse of duration $6\beta^{-1}$. The FID signal (b) is extracted by fitting the experimental data ((a), grey line). The parameters of the CHS are $\mu = 30$, $\beta = 0.08 \mu\text{s}^{-1}$ and $\Omega_0/\mu\beta = 0.9$. The coherence lifetime is $T_2 = 8\beta^{-1}$.

have demonstrated that efficient population transfer by a CHS pulse is related to the adiabatic condition. This has led us to show that a CHS pulse can adiabatically excite atoms over a spectral interval $2\mu\beta$ significantly larger than the maximum Rabi frequency, provided $\mu \gg 1$. Then, when the adiabatic condition is fulfilled we have simply assumed that the Bloch vector keeps locked to the driving vector all along the excitation pulse. This way, we get physical insight into the process. We get better understanding of its spectral selectivity and of limiting factors, such as coherence lifetime and finite duration. This approach is confirmed by numerical solution of the Bloch equations and experimental results. For the first time in the optical domain, using CHS excitation, we have experimentally demonstrated population transfer close to 100%, not only population inversion. By resorting to FID signal analysis, we have been able to follow the Bloch vector evolution along the excitation process. Finally, we have proposed a new technique to prepare the atoms in a superposition state. By the way, the adiabatic model approach still suggests another procedure to drive the Bloch vector from any initial position to an arbitrary final direction. This could be accomplished by first growing the driving vector along the Bloch vector, until the latter is locked. This is made possible with our present laser phase and amplitude control techniques. Then one is free to adiabatically orient the driving vector to the desired direction. Finally the field can be switched off abruptly. In summary, we have clarified the conditions in which CHS excitation can be used in the framework of quantum information, either to build C-NOT gates [1] or to drive 3-level system [18] in the prospect of quantum storage.

This work was supported by the European Community Information Society Technologies Program under contract IST-2000-30064. We are grateful to Professor Klaus Mølmer for suggesting the use of complex hyperbolic secant for efficient frequency selective state swapping.

References

1. N. Ohlsson, R.K. Mohan, S. Kroll, *Opt. Commun.* **201**, 71 (2002)
2. J.J. Longdell, M.J. Sellars, e-print [arXiv:quant-ph/0208182](https://arxiv.org/abs/quant-ph/0208182); see also J.J. Longdell, Ph.D. thesis, Australian National University, 2003 <http://eprints.anu.edu.au/archive/00002321/>
3. K. Ichimura, *Opt. Commun.* **196**, 119 (2001)
4. R.W. Equall, Y. Sun, R.L. Cone, R.M. Macfarlane, *Phys. Rev. Lett.* **72**, 2179 (1997)
5. E. Fraval, M.J. Sellars, J.J. Longdell, *Phys. Rev. Lett.* **92**, 77601 (2004)
6. G.J. Pryde, M.J. Sellars, N.B. Manson, *Phys. Rev. Lett.* **84**, 1152 (2000)
7. J. Wesenberg, K. Mølmer, *Phys. Rev. A* **68**, 12320 (2003)
8. M.S. Silver, R.I. Joseph, D.I. Hault, *Phys. Rev. A* **31**, 2753 (1985)
9. F.C. Spano, W.S. Warren, *Phys. Rev. A* **37**, 1013 (1988)
10. M.R. Fetterman, J.C. Davis, D. Goswami, W. Yang, W.S. Warren, *Phys. Rev. Lett.* **82**, 3984 (1999)
11. M.R. Fetterman, Ph.D. thesis, Princeton University, 1999
12. V. Crozatier, F. de Seze, L. Haals, F. Bretenaker, I. Lorgeré, J.-L. Le Gouët, *Opt. Commun.* **241**, 203 (2004)
13. V.S. Malinovsky, J.L. Krause, *Eur. Phys. J. D* **14**, 147 (2001)
14. N.V. Vitanov, B.M. Garraway, *Phys. Rev. A* **53**, 4288 (1996)
15. D. Allen, J.H. Eberly, *Optical resonance and two-level atoms* (Wiley, New York, 1975)
16. A. Bambini, P.R. Berman, *Phys. Rev. A* **23**, 2496 (1981)
17. F.T. Hioe, *Phys. Rev. A* **30**, 2100 (1984)
18. I. Roos, K. Mølmer, *Phys. Rev. A* **69**, 22321 (2004)
19. Y. Sun, G.M. Wang, R.L. Cone, R.W. Equall, M.J.M. Leask, *Phys. Rev. B* **62**, 15443 (2000)
20. G.J. Pryde, M.J. Sellars, N.B. Manson, *Phys. Rev. Lett.* **84**, 1152 (2000)
21. F. de Seze, V. Lavielle, I. Lorgeré, J.-L. Le Gouët, *Opt. Commun.* **223**, 321 (2003)
22. D. Rourke, Ph.D. thesis, University of Nottingham, 1992, <http://www.magres.nottingham.ac.uk/~rourke/phd/>
23. N.W. Carlson, W.R. Babbitt, Y.S. Bai, T.W. Mossberg, *Opt. Lett.* **9**, 232 (1984)